

Magnetohydrodynamic Simulation of a Halo Coronal Mass Ejection on September 10, 2014*

YINGJIE ZHU¹

¹Department of Climate and Space Sciences and Engineering, University of Michigan, Ann Arbor, MI 48109, USA

ABSTRACT

The coronal mass ejection (CME) is one of the major solar eruptions that significantly impacts on the terrestrial space weather environment. To have a better understanding of CME eruption and propagation in the solar corona and ambient solar wind, I was assigned to simulate a halo CME eruption on September 10, 2014, using the Alfvén Wave Solar Wind Model (AWSOM) and the Eruptive Events Generator, Gibson and Low (EEGGL). I ran two steady-state solar wind solutions using different Poynting flux constant at the inner boundary: 0.37×10^6 (PF0.37) and 1.0×10^6 $\text{J} \cdot \text{m}^{-2} \cdot \text{s}^{-1} \cdot \text{T}^{-1}$ (PF1.0). The synthetic EUV images of the simulated solar corona are fainter than the SDO/AIA and STEREO/SECCHI EUVI observations. The solar wind condition at 1 au in PF0.37 model is closer to observed values, while the steady-state solar wind is much denser in PF1.0 model. The CME simulation can reproduce some features in remote-sensing observations, e.g., leading edge in SOHO/LASCO C2 and C3 coronagraph and coronal dimming in SDO/AIA 171 Å passband. The simulated CME shock arrives at the earth 12 hours later in the PF0.37 model and three days later in the PF1.0 model due to the denser solar wind condition and small flux rope magnetic field strength. Parameter optimization in flux rope magnetic field strength and post-processing of the input photospheric magnetogram are needed to improve the simulation results.

Keywords: Solar coronal mass ejections (310), Magnetohydrodynamical simulations (1966), Solar wind (1534), Interplanetary medium (825)

1. INTRODUCTION

Coronal mass ejections (CMEs) are sudden eruptions of coronal plasma structures into the interplanetary space. The bulk motion of the ejected plasma and the magnetic field carried by that plasma create significant disturbances to the ambient steady solar wind flows and the space weather environment of the planets. Large CMEs targeting the earth, so-called halo CMEs, may result in disastrous space weather events, which threaten the communication, power transmission, navigation, aviation, and other industries. Therefore understanding how the CMEs erupt in the solar corona and propagate in the interplanetary space is one of the critical topics in solar physics research.

The properties of the observed CMEs vary in 2-3 orders magnitudes. The apparent velocity of the CME vary from $20 - 2500 \text{ km} \cdot \text{s}^{-1}$ (Webb & Howard 2012). The acceleration of the CMEs by the Lorentz force occurs in the lower corona, followed by intermediate and gradual acceleration at larger heliocentric distance

$> 5 R_{\odot}$ (Aschwanden 2019). A statistical study carried out by Bein et al. (2011) shows that 74% of CMEs are accelerated to the maximum speed below $0.5 R_{\odot}$ from the surface of the sun. One CME eruption can carry a mass in a range of $10^{12} - 10^{16} \text{ g}$ and total mechanical energy of $10^{27} - 10^{31} \text{ erg}$ (Vourlidas et al. 2010). In white-light images taken by coronagraphs, a typical CME reveals a three-part structure: leading edge, dark cavity, and bright filament (Illing & Hundhausen 1985).

Highly twisted or sheared magnetic structures like magnetic flux ropes and sheared arcades are considered as the progenitors of the CMEs, where the nonpotential energy released in the eruption is restored (Chen 2011). Non-linear force-free field (NLFFF) extrapolations of the photospheric magetic fields suggest the existence of flux ropes in some active regions before flare/CME eruptions (e.g., Yan et al. 2001; Schrijver et al. 2008). Other features in extreme ultraviolet (EUV) observations of solar corona like filament, coronal cavities, sigmoids, and hot channels also support the existence of magnetic flux ropes (Cheng et al. 2017). Different models have been proposed to explain the triggering processes of the progenitors (Chen 2011), for example: tether-cutting or flux cancellation (e.g., Moore & Labonte 1980), shearing mo-

* Note that this is not a peer-reviewed paper. It is a report of the final project of SPACE 597 taught by Prof. Tamas Gombosi.

tions (e.g., Jacobs et al. 2006), magnetic breakout (Antiochos et al. 1999), emerging flux (Chen & Shibata 2000), and various types of instabilities (e.g., kink instability: Sakurai (1976), torus instability: Kliem & Török (2006), and catastrophe: Lin et al. (1998)).

Magnetohydrodynamics (MHD) simulations have been widely used in investigating the initiation (e.g., Amari et al. 2003a,b; Török & Kliem 2003) and propagation of CMEs (e.g., Riley et al. 2003) with pre-existing flux ropes or flux ropes forming during the eruption.

The Block Adaptive Tree Solar-Wind Roe Upwind Scheme (BATS-R-US) code (Powell et al. 1999) and later on Space Weather Modeling Framework (SWMF, Tóth et al. 2005, 2012) have been used to simulate the CME eruption and propagation to 1 astronomical unit (au) since the early 2000s. Groth et al. (2000) simulated a space weather event by introducing a localized isothermal density enhancement in the steady-state solar wind solution. The loss of equilibrium of a Titov and Démoulin flux rope (Titov & Démoulin 1999) was studied by Rousset et al. (2003). Manchester et al. (2004a,b) adopted a Gibson and Low (GL) flux rope (Gibson & Low 1998) anchored at the photosphere to initialize the CME and generated intense geomagnetic storms in the simulation. The interaction between two CMEs and the CME's energy density evolution is also studied by Lugaz et al. (2005a,b). Lugaz et al. (2007) utilized the coronal magnetic field reconstructed from the photospheric magnetogram to replace the simplified steady-state solar wind model. Manchester et al. (2008) initiated two CMEs in sequences to model the CME event on October 28, 2008, and reproduced white-light images of the CME eruption. Cohen et al. (2008, 2009) obtained the CME parameters from both magnetogram and coronagraph observations and produced the EIT waves caused by the CME eruption. The magnetic reconnection during the CME eruption is also investigated by Cohen et al. (2010); Lugaz et al. (2011).

After that, the Alfvén Wave Solar Wind Model (AWSOM, van der Holst et al. 2010, 2014) was developed and became the solar corona and inner heliosphere module of the SWMF. Manchester et al. (2012) utilized the two-temperature feature of AWSOM to study the coupled evolution of electrons and protons in CME-driven shocks. The discrepancy in simulated CME-driven shock parameters between one-temperature and two-temperature models is discussed in Jin et al. (2013). Lugaz et al. (2013) studied the interaction between two CMEs and how the magnetic reconnection determines the CME structures during the propagation. The evolution of the magnetic flux ropes and magnetic clouds are further studied in Manchester et al. (2014a,b). The im-

pact of flux rope eruption to adjacent solar structures is investigated by Jin et al. (2016). Recently, a new Eruptive Events Generator, Gibson and Low (EEGGL) was developed (Jin et al. 2017b), which shows the capability to reproduce a vast number of CME features in both the lower corona and heliosphere (Jin et al. 2017a).

A halo CME was first observed in the C2 images of the Large Angle Spectroscopic Coronagraph (LASCO, Brueckner et al. 1995) on board *Solar and Heliospheric Observatory* (SOHO; Domingo et al. 1995) at 18:02 UT on September 10, 2014. The CME was triggered by an X1.6 class flare that erupted in NOAA active region (AR) 12158 at 17:21 UT and peaked at 17:45 UT. The CDAW database recorded a CME linear speed of $1267 \text{ km} \cdot \text{s}^{-1}$, while the SWRC database provided a speed of $\sim 1400 \text{ km} \cdot \text{s}^{-1}$. It took the CME shock less than 48 hours to arrive at the earth at 15:26 UT on September 12, 2014. The CME triggered a geomagnetic storm with a maximum Kp index of 7.0 and a minimum Dst of -87.0 nT .¹

In this project, I was assigned to simulate the halo CME erupting on September 10, 2014, using AWSOM and EEGGL, and compare the simulation with both in-situ measurements at 1 au and remote-sensing observations. The rest of the report will be organized in the following way: I will introduce the AWSOM, EEGGL and modeling procedures in Section 2; the simulation results and comparison to observations will be presented in Section 3; a naive discussion of the results will be carried out in Section 4; the section 5 will provide a summary to the report.

2. METHODOLOGY

2.1. AWSOM

Alfvén Wave Solar Wind Model (AWSOM, van der Holst et al. 2010, 2014) is the Solar Corona (SC) and Inner Heliosphere (IH) components of the Space Weather Modeling Framework (SWMF, Tóth et al. 2005, 2012), which extends for the upper chromosphere to the corona and the heliosphere. AWSOM solves the three-temperature MHD equations for isotropic electron temperature and anisotropic proton temperature to simulate the solar corona and inner heliosphere plasma dynamics. Alfvén wave equations describe the propagation, reflection, and dissipation of Alfvén waves to address the coronal heating and solar wind acceleration.

¹ By the way, I found this event has been studied by Manchester et al. (2019) when I was writing this report. The comparison between my naive simulation and Manchester et al. (2019) is not included in this report for time reasons. It is also because Manchester et al. (2019) is an AGU poster/presentation without direct access.

To simulate the coronal magnetic field structures, a photospheric magnetogram is extrapolated as the pre-specified boundary conditions. The Poynting flux at the inner boundary is proportional to the magnetic field strength at the inner boundary by a constant. AWSOM used adaptive mesh refinement (AMR) blocks to resolve the heliospheric current sheet. At the last of the steady-state run, there are $\sim 4.5 \times 10^6$ cells in SC and 10^7 cells in IH.

2.2. EEGGL

Eruptive Events Generator, Gibson and Low (EEGGL, Jin et al. 2017b) is an automatic tool to generate analytical flux rope parameters by giving the footprint locations on a synoptic photospheric magnetogram. The EEGGL adopts the flux rope model proposed Gibson & Low (1998) to find the flux rope parameters under a magnetohydrostatic condition. Five parameters describe the flux rope: a stretching parameter a controlling the shape of the flux rope, the distance r_1 from the solar surface to flux rope torus center, the flux rope radius r_0 , magnetic field strength a_1 inside the flux rope, and the flux rope helicity.

When the flux rope parameters are determined, the flux rope density and magnetic field strength are directly superposed to background coronal density and magnetic field. The strong magnetic field pressure inside the flux rope creates an unstable system and drives the eruption immediately. Jin et al. (2017b) suggests several advantages of utilizing an imbalanced force flux rope model, including no energy build-up stage before eruption, dense plasma, and low-density cavity structure above the polarity inversion line (PIL), and controllable CME eruption speed.

2.3. Modeling Setup

In this project, I ran the AWSOM simulations on the supercomputer Cheyenne². First, I pre-processed a synoptic photospheric magnetogram Global Oscillation Network Group (GONG, Harvey et al. 1996) (see Figure 1) with Finite Difference Iterative Potential-field Solver (FDIPS, Tóth et al. 2011) to create the input of AWSOM runs. Second, I ran the AWSOM simulation with local time stepping to obtain a steady-state solar wind solution. I obtained two steady-state solutions using two different Poynting flux to magnetic field strength ratio: 0.37×10^6 and $10^6 \text{ J} \cdot \text{m}^{-2} \cdot \text{s}^{-1} \cdot \text{T}^{-1}$.

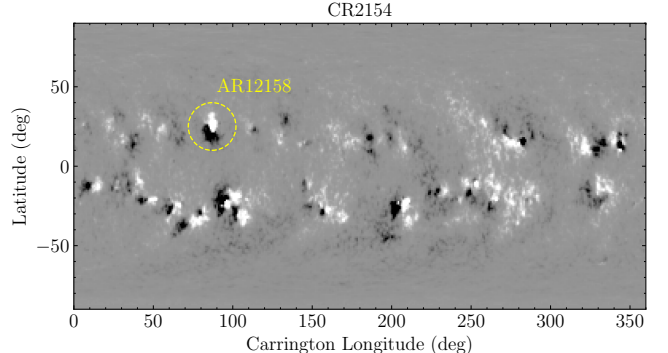


Figure 1. The GONG synoptic photospheric magnetogram of CR2154 used in the simulation. The AR12158 is marked in the yellow circle.

The `#MINIMUMRADIALSPEED` is used to avoid inflows in the solar wind. Then I used EEGGL to obtain the CME flux rope parameters from the GONG magnetogram, inserted the flux rope in the steady-state solution, and restarted the AWSOM to simulate the eruption of the CME in the ambient solar wind.

3. RESULTS

3.1. Steady-state Solution

I ran two steady-state simulations with Poynting flux to magnetic field strength ratio equal 0.37×10^6 (PF0.37) and $10^6 \text{ J} \cdot \text{m}^{-2} \cdot \text{s}^{-1} \cdot \text{T}^{-1}$ (PF1.0). In order to check the consistency of the AWSOM simulation, I used `compare_remote.pro` routine to compare the synthetic solar EUV images with the remote-sensing observations from *Atmospheric Imaging Assembly* (AIA, Lemen et al. 2012) on board *Solar Dynamic Observatory* (SDO, Pesnell et al. 2012) and SECCHI/EUVI (Howard et al. 2008) on board STEREO-A/B spacecraft (Kaiser et al. 2008). The solar wind condition at 1 au in our simulation is also compared with OMNI data as extracted from NASA/GSFC's OMNI data set through OMNI-Web.

The Figure 2 shows the comparison between the simulation and SDO/AIA observations in 6 different passbands, which are sensitive to different temperatures: 94 Å (Fe XVIII, $\log T = 6.8$), 131 Å (Fe VIII, XX, XXIII, 5.6, 7.0, 7.2), 171 Å (Fe IX, 5.8), 193 Å (Fe XII, XXIV, 6.1, 7.3), 211 Å (Fe XIV, 6.3), 335 Å (Fe XVI, 6.4). The active region and ambient solar corona are brighter than the quiet solar corona in the simulations. The simulations cannot reproduce fine structures in the active regions in the real SDO/AIA observations. The southern polar coronal holes observed by SDO/AIA is reproduced in all the synthetic AIA images. The solar corona in PF0.37 model is fainter than that in PF1.0 model. The synthetic images of the PF0.37 model reveal a coronal hole

² Computational and Information Systems Laboratory. 2019. Cheyenne: HPE/SGI ICE XA System (Climate Simulation Laboratory). Boulder, CO: National Center for Atmospheric Research. doi:10.5065/D6RX99HX.

at the north pole that is not presented in observations. The synthetic AIA 131 and 171 Å images of the PF1.0 model are most similar to the SDO/AIA observations.

The comparison between the STEREO/SECCHI EUVI observations are shown in Figure 3. Since STEREO-A and B are close to each other at the far side of the sun, only the comparison with STEREO-A observations is shown. The EUVI 195 Å emission is mainly contributed by Fe XII, which is similar to SDO/AIA 193 Å. EUVI 284 Å is dominated by the emission from Fe XV which peaks at $\log T = 6.3$. The results are similar to the SDO/AIA images. All the synthetic EUVI images reveal an equatorial coronal hole and a coronal hole at the south pole. The EUVI images of PF0.37 model is dimmer than the PF1.0 model, and the bright active regions, especially in the hotter EUVI 284 Å channel, cannot be reproduced by the simulations.

I also used the `compare_in-situ.pro` to compare the simulations with in-situ measurements of STEREO observations at the far side of the sun and the OMNI data. The Figure 4 shows the comparison between the modeled solar wind condition at 1 au with the OMNI database. The strong fluctuations in the solar wind condition caused by CMEs are not included in the steady-state solution. The model cannot reproduce the small changes in the solar wind condition because of the coarse grid. Generally speaking, the PF0.37 model shows a better consistency with the OMNI database, especially in the solar wind radial velocity u_r at $\sim 400 \text{ km} \cdot \text{s}^{-1}$. The number density of the background solar wind in PF0.37 model ($\sim 10 \text{ cm}^{-3}$) is close to the OMNI data, while the number density in PF1.0 model of $\sim 20 - 30 \text{ cm}^{-3}$ is much larger than the observations. The temperature at 1 au in both PF0.37 and PF1.0 models are smaller than the observed values of $\sim 10^5 \text{ K}$. The total magnetic field strength in the PF1.0 model ($\sim 5 \text{ nT}$) is larger than that in the PF0.37 model and closer to the observed values from the OMNI database.

The comparison with the STEREO-A and B observations at the far side of the sun is demonstrated in Figure 5 and 6. The overall solar wind radial velocity u_r in PF0.37 model is similar to the observed values $\sim 400 \text{ km} \cdot \text{s}^{-1}$ during the eruption while the radial velocity u_r in PF1.0 decreases to $\sim 200 \text{ km} \cdot \text{s}^{-1}$ at the same time. The particle density in the PF1.0 model is still much larger than the PF0.37 model and the observed values. The temperature in PF1.0 model matches the STEREO observations better, especially during September 4 - 9. Similarly, the total magnetic field in the PF1.0 model of 5 nT is larger than that in PF0.37, but still smaller than the observed values of $\sim 5 \text{ nT}$.

3.2. Magnetic Flux Rope Parameters

I determined the flux rope parameters from the GONG synoptic magnetogram using EEGGL. The only additional input to EEGGL is the position of the positive and negative footprints. The CME flux rope parameters are shown in Table 1. Since I have no experience in using Tecplot to illustrate the 3-D flux rope, a 2-D vector plot of the photospheric magnetic field generated in the EEGGL run is shown in Figure 7.

3.3. CME in White-light Coronagraph

I compared the synthetic SOHO/LASCO white-light images of the CME propagating in the lower solar corona with the SOHO/LASCO observations. I used the processed SOHO/LASCO images from Helioviewer because I am not familiar with SOHO/LASCO data reduction and enhancement. Some of my attempts to enhance the SOHO/LASCO level 1 data are presented in Section A. The C2 coronagraph has a field of view (FOV) from $2.0 R_\odot$ to $6.0 R_\odot$ and C3 coronograph has a FOV from $3.7 - 32 R_\odot$. I did not include the comparison with the STEREO/SECCHI COR data because the STEREO-A/B are at the far side of the sun, so their observations do not have much information about the 3-D structure of the CME.

The SOHO/LASCO C2 and C3 observations of the CME was shown in Figure 8. The leading edge of the CME first appeared in the C2 FOV at 18:00 UT. The halo shaped leading edge was entirely caught by C2 FOV at 18:36 UT. Another small eruption is observed in C2 at 20:48 UT. The C3 images also illustrate the halo structures of the CME.

The synthetic SOHO/LASCO C2/3 images from PF0.37 and PF1.0 models are shown in Figure 9 and 10 respectively. Both the PF0.37 and PF1.0 C2/C3 images reveal the halo shaped leading edge of the CME (illustrated by the green arrow), which shows remarkable consistency in the spatial position with the SOHO/LASCO observations. The linear velocity of the leading edge in PF0.37 model is faster than that in PF1.0 model, but the linear velocity in the simulations is slower than the observed values. Besides, there is an unexpected "brightening remnant" revealed in both C2/C3 images of PF0.37 and PF1.0 models (illustrated by the blue arrow). I will discuss the formation of this structure in Section 4.

3.4. CME-Caused Coronal Dimming

The coronal dimming refers to the decrease of coronal intensity in EUV or X-ray passband after CME eruption, which is commonly observed in nearly all CMEs (Mason et al. 2014). It is directly caused by the coronal

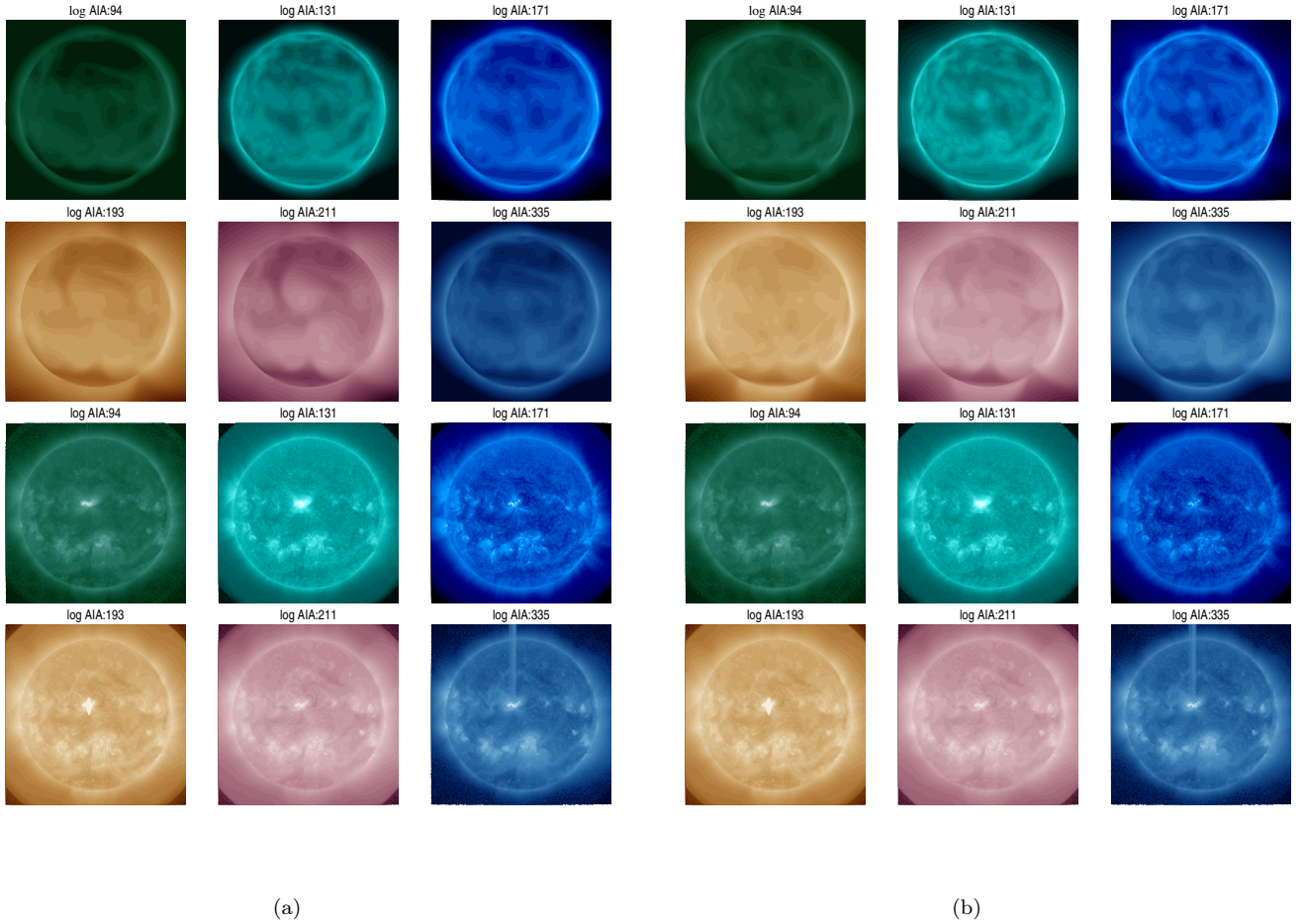


Figure 2. Comparison between the synthetic solar EUV images from PF0.37 (a) and PF1.0 (b) steady-state solution with SDO/AIA observations.

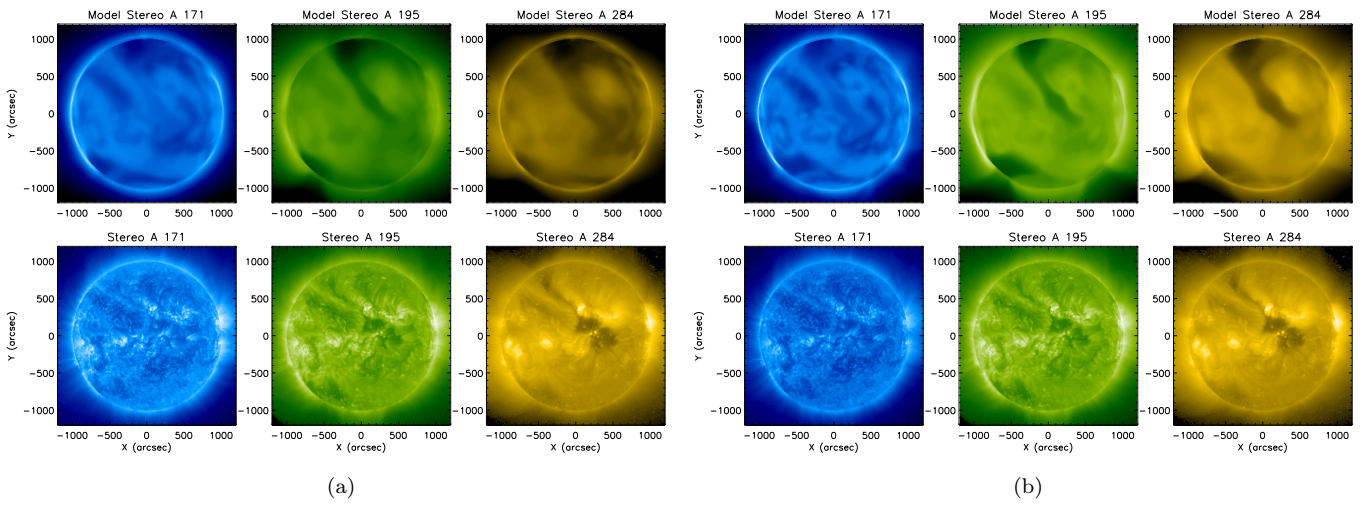


Figure 3. Comparison between the synthetic solar EUV images from PF0.37 (a) and PF1.0 (b) steady-state solution with STEREO/SECCHI EUVI observations. Since STEREO-A and B are close to each other at the far side of the sun, only the comparison with STEREO-A observations is shown.

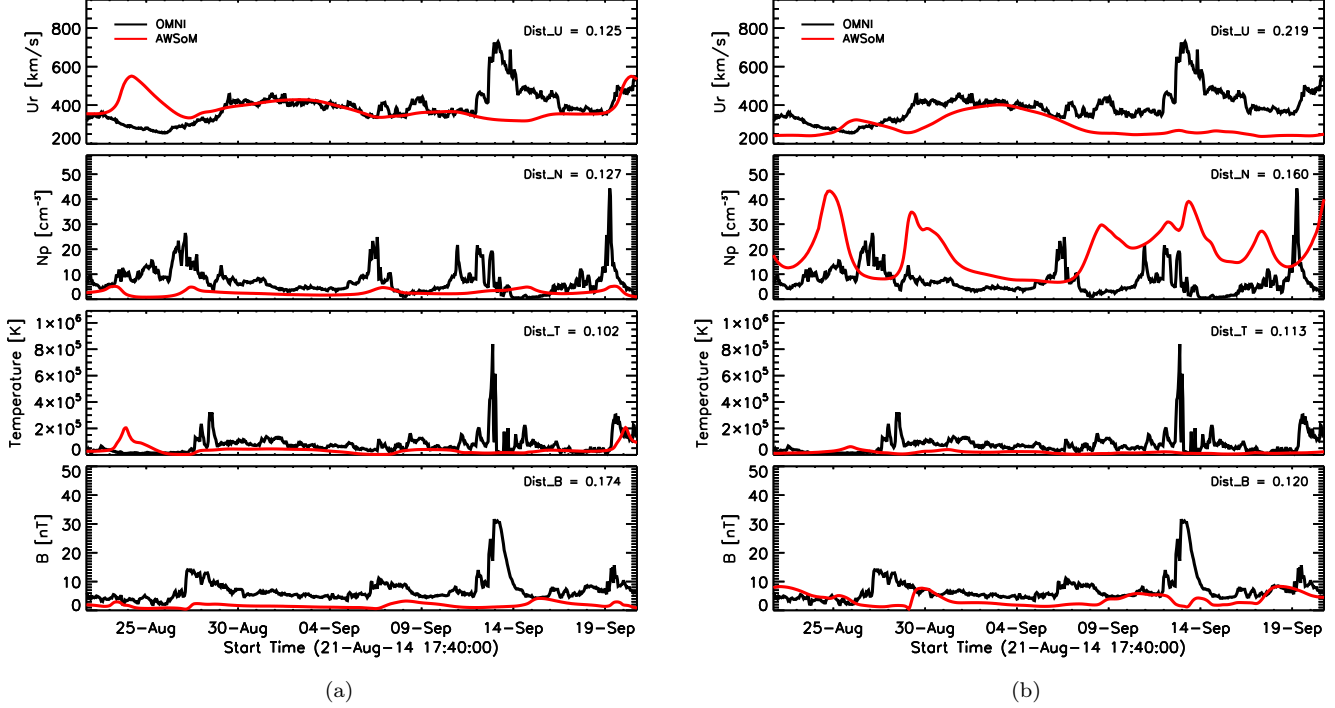


Figure 4. Comparison between the solar wind condition from PF0.37 (a) and PF1.0 (b) steady-state solution with OMNI database.

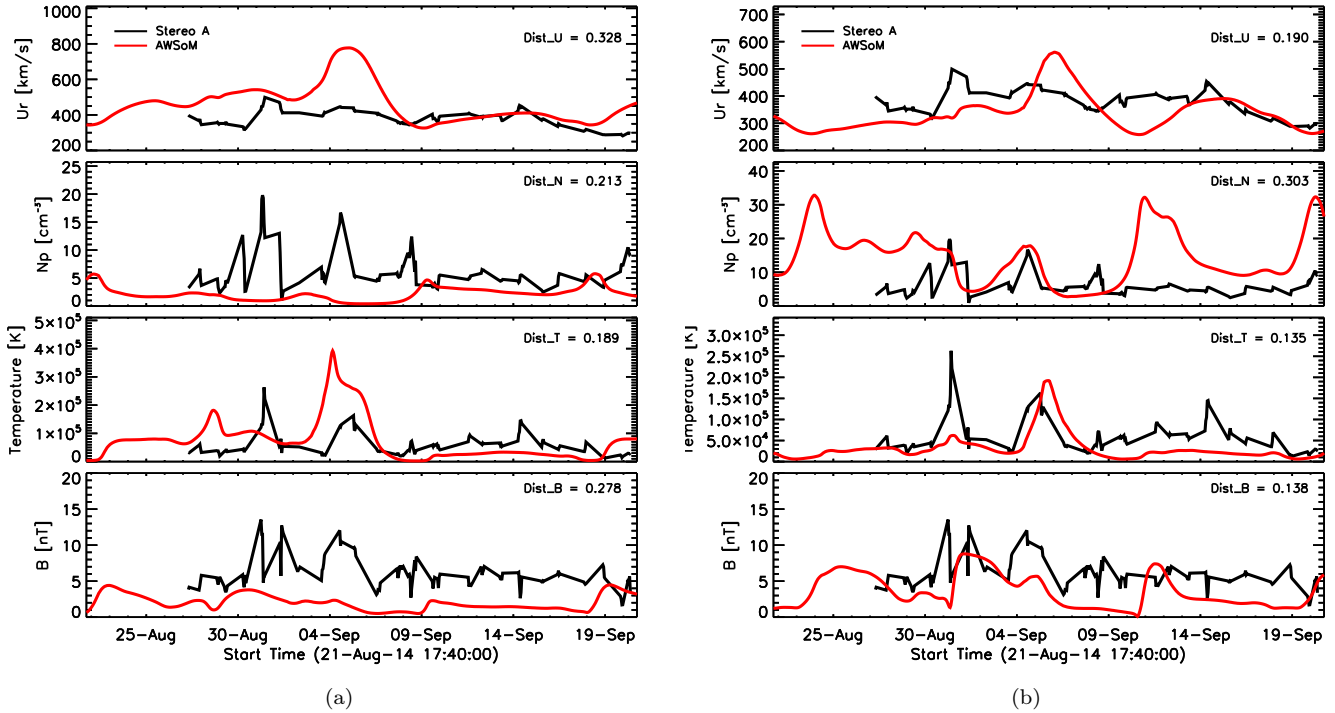
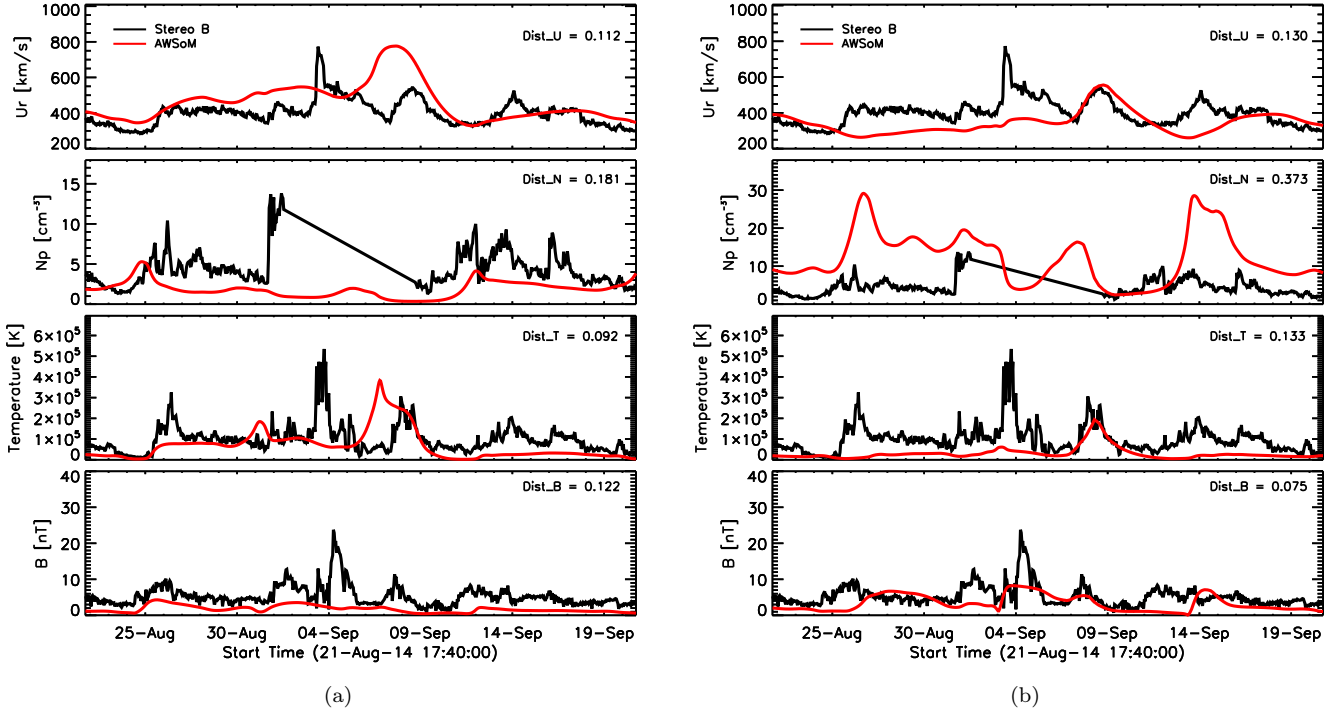


Figure 5. Comparison between the solar wind condition from PF0.37 (a) and PF1.0 (b) steady-state solution with STEREO-A measurements.



(a)

(b)

Figure 6. Comparison between the synthetic solar EUV images from PF0.37 (a) and PF1.0 (b) steady-state solution with STEREO-B measurements.

Long (deg)	Lat (deg)	Orientation (deg)	B	Radius	Stretching	Apex Height (R_{\odot})
87.50	14.52	255.96	-26.14	0.58	0.60	0.78

Table 1. CME flux rope parameters retrieved from EEGGL.

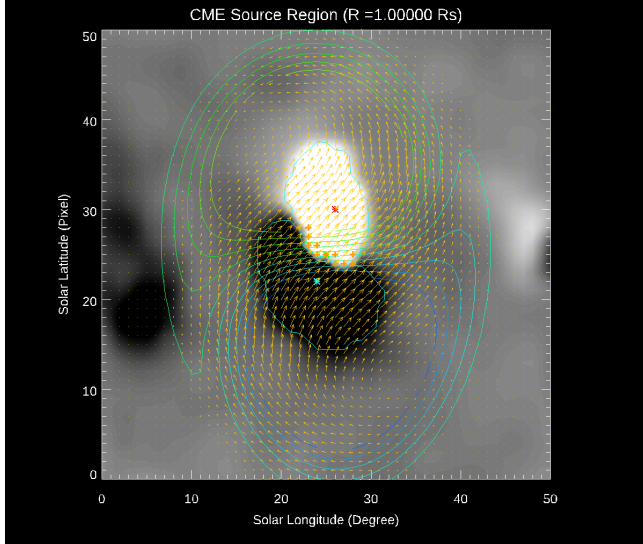


Figure 7. The photospheric magnetic field of AR12158 in GONG synoptic map and the photospheric magnetic field of the flux rope footprints.

mass loss due to the CME eruption (Tian et al. 2012).

Here I compared the intensity change of the SDO/AIA 171 Å passband before and after the eruption in both simulation and observations. The results are shown in Figure 11. The SDO/AIA observation shows the brightening of the post flare loops and the dimming of the ambient solar corona (illustrated by the yellow circle). The PF0.37 and PF1.0 models show the brightening at the center of the active region and intensity decrease in the northern hemisphere. The dimming region in PF0.37 model is more extensive than those in the PF1.0 model and observations. The coronal dimming gradually recovers in both simulation and observations, the dimming in the high latitude regions in the simulation last for more than 10 hours.

3.5. CME Shock Propagation in Inner Heliosphere

The CME shock and ambient solar wind properties in the equatorial cut at 40 h after the CME eruption are shown in Figure 12. The ambient solar wind density in PF0.37 model is much smaller than that in PF1.0 model, which has already been shown in the steady-state solar wind condition in Figure 4. The CME shock at 40

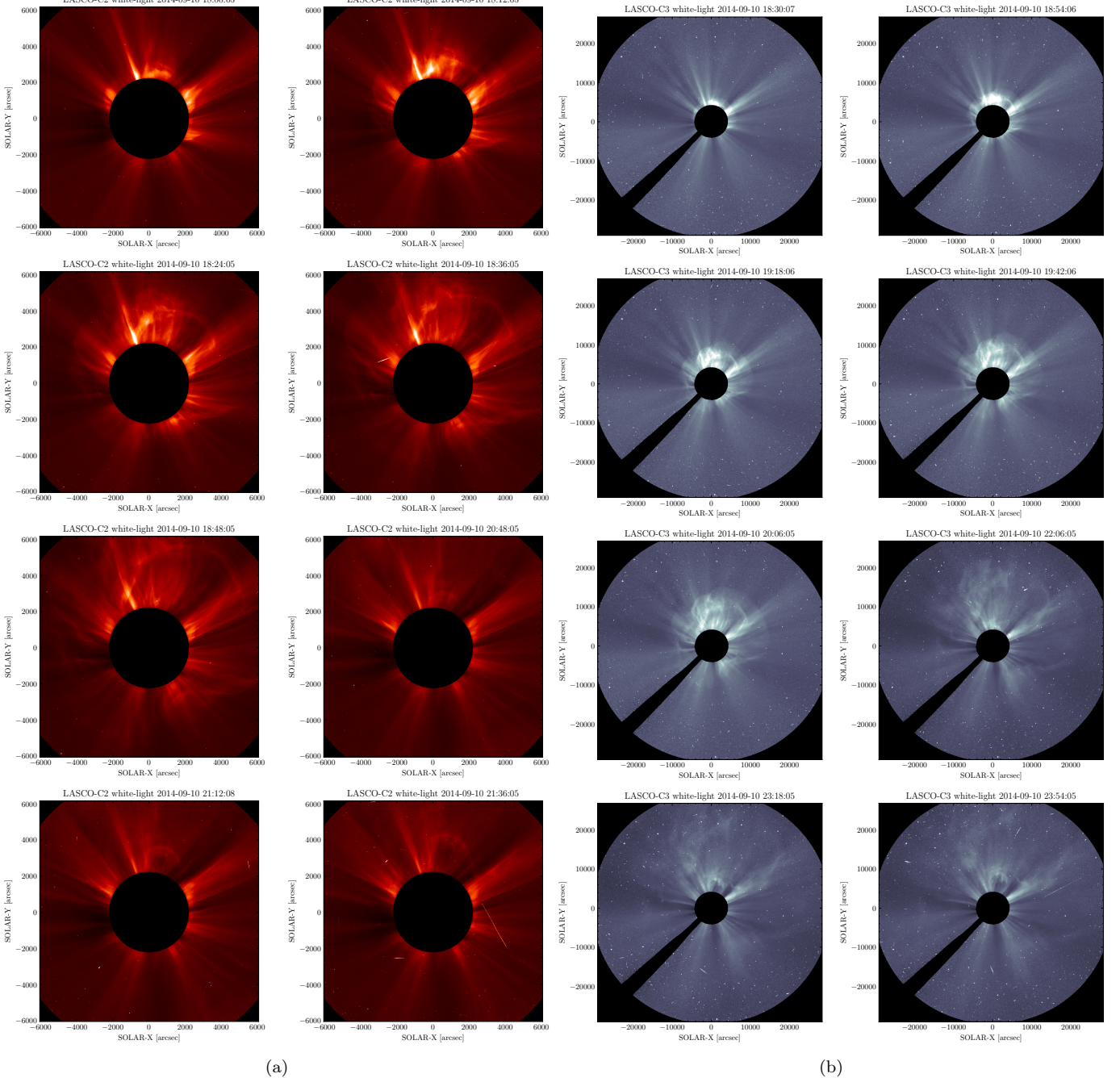


Figure 8. CME white-light observations from SOHO/LASCO C2 (a) and C3 (a) coronagraphs.

h has a mass density of $\sim 10^{-22} \text{ g} \cdot \text{cm}^{-3}$ in PF0.37 model. The radial velocity of the CME shock in PF0.37 is $\sim 700 \text{ km} \cdot \text{s}^{-1}$, while the CME shock in PF1.0 model is much slower with a radial velocity of $\sim 400 \text{ km} \cdot \text{s}^{-1}$. The differences between the radial velocity in the two models can also be verified from the shock's position at 40 h after the eruption. Part of the CME propagates into a streamer in PF0.37 model, which is similar to the results in Jin et al. (2017a). The proton temperature of

the CME shock in PF0.37 model is $\log T \sim 6.2$, which is higher than the proton temperature of $\log T \sim 5.5$ in PF1.0 model. The total magnetic field strengths at the shock front are 10^{-4} G and $10^{-3.5} \text{ G}$ for PF0.37 and PF1.0 model respectively.

3.6. CME Shock Conditions at 1 au

The simulated CME shock properties at 1 au from two models are compared with the OMNI database in

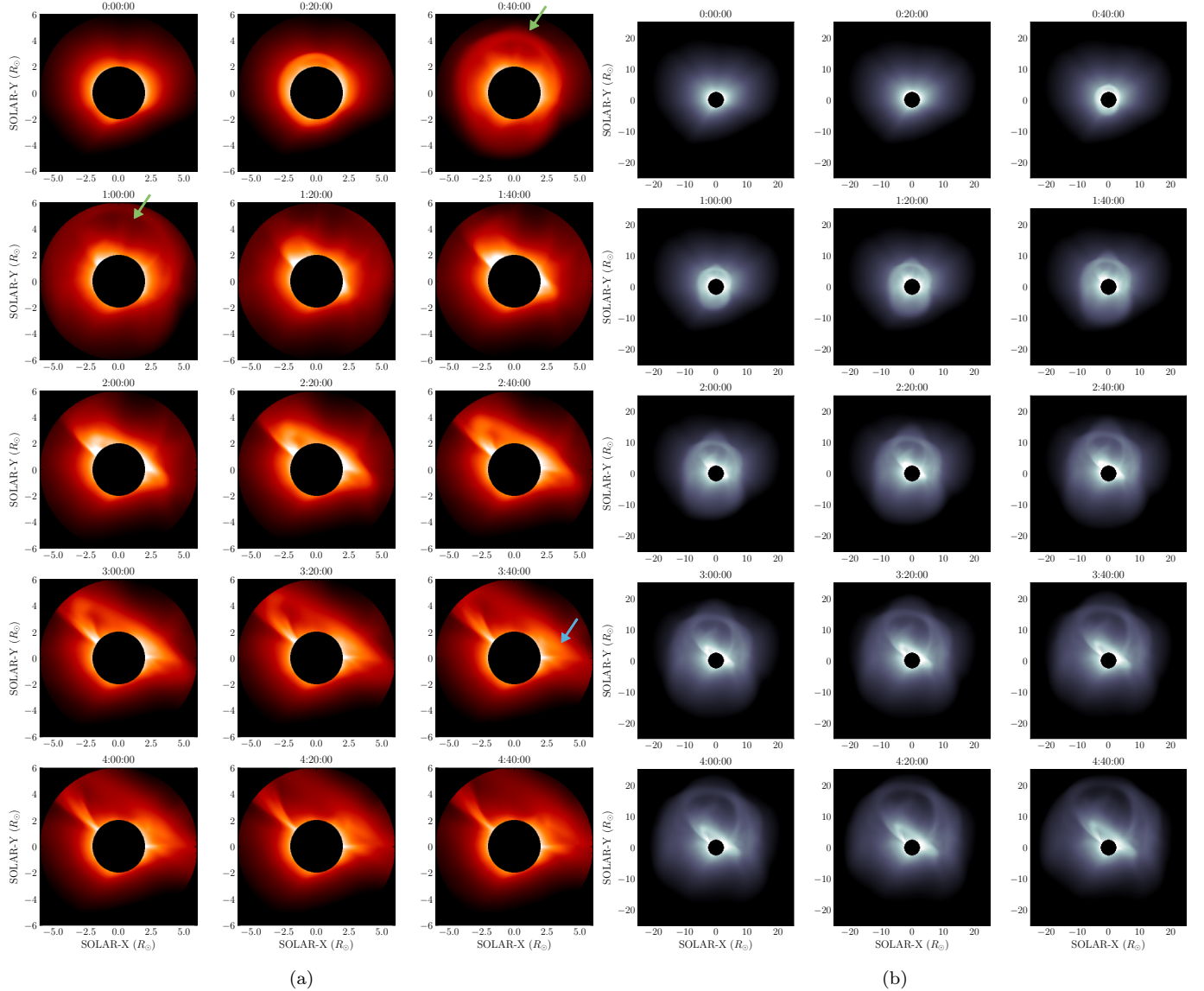


Figure 9. Synthetic white-light SOHO/LASCO C2 (a) and C3 (a) observations in PF0.37 model. Green arrow: leading edge; Blue arrow: a brightening remnant.

Figure 13. The arrival time of CME shock in PF0.37 model at the earth is later than the real arrival time by ~ 10 hours. The solar wind radial velocity jumps from $350 \text{ km} \cdot \text{s}^{-1}$ to $500 \text{ km} \cdot \text{s}^{-1}$, which is still smaller than the observed $\sim 700 \text{ km} \cdot \text{s}^{-1}$. The number density jumps from 5 to 15 cm^{-3} , which is slightly higher than the observed values. The temperature increase dramatically from less than 10^5 K to $\sim 1.1 \times 10^6 \text{ K}$, which is larger than the observed values of $9 \times 10^5 \text{ K}$. The total magnetic field increases by $\sim 10 \text{ nT}$, which is smaller than the observed increase by 25 nT.

In the PF1.0 model, the CME arrives three days later than real observations due to the small radial velocity caused by large ambient solar wind density. The radial

velocity increase from 200 to $400 \text{ km} \cdot \text{s}^{-1}$, smaller than observed value $\sim 700 \text{ km} \cdot \text{s}^{-1}$. The number density increases unrealistically to 70 cm^{-3} in the simulation. The proton temperature increases to $\sim 3 \times 10^5 \text{ K}$, which is smaller than the observed values. The less proton temperature increase in the simulation may come from the CME shock's insufficient heating due to the slow propagation speed. The total magnetic field increases by $\sim 20 \text{ nT}$, which is the only quantity consistent with previous measurements.

4. DISCUSSIONS

4.1. Faint Corona

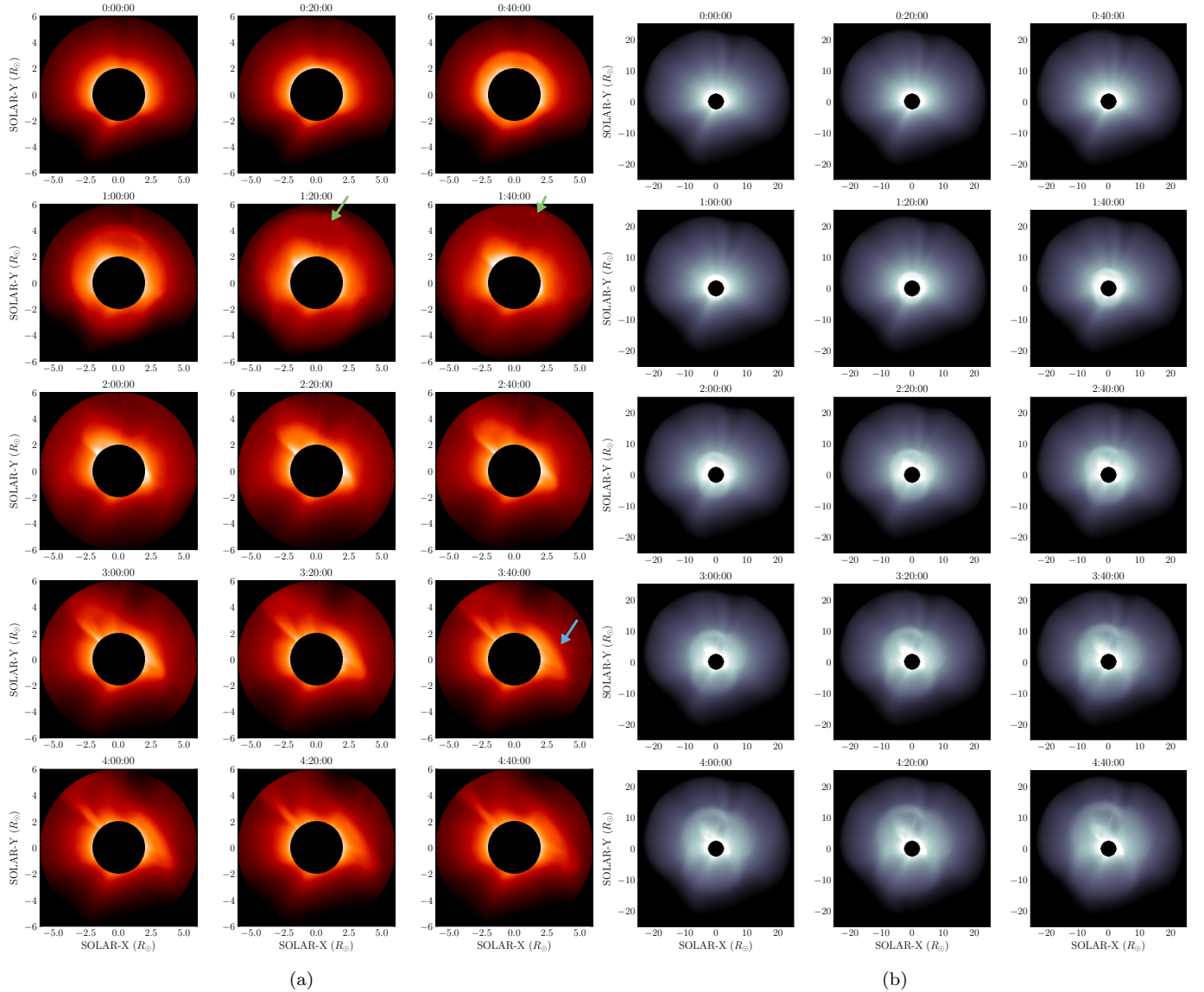


Figure 10. Synthetic white-light SOHO/LASCO C2 (a) and C3 (a) observations in PF1.0 model. Green arrow: leading edge; Blue arrow: a brightening remnant.

Both the simulated solar corona in PF0.37 and PF1.0 models are fainter than the SDO/AIA observations and the bright active region features can only be distinguished in AIA 131 Å and AIA 171 Å, which is similar to the results in Sachdeva et al. (2019). Since the AIA 131 Å has a low temperature contribution from Fe VIII ($\log T = 5.6$) and AIA 171 Å is contributed by Fe IX emission which peaks at $\log T = 5.8$, I suggest the solar corona in the simulation is still cooler than the real observations so that the bright features in the hot AIA channels (e.g., AIA 94 Å and AIA 211 Å) cannot be reproduced. Besides, since the coronal magnetic field is extrapolated from a synoptic photospheric magnetogram describing the entire Carrington rotation, it's

difficult for the model to reproduce the instantaneous features in the solar corona.

Jin et al. (2017a) simulated the steady-state solar corona of CR2107 and reproduced most of the brightening active regions, even in the hot AIA channels like AIA 211 Å. However, they still reported that the synthetic intensity in the cooler passbands like AIA 171 Å is two times larger than the observed values while the hot AIA 211 Å emission is underestimated by a factor of five in the simulation, which suggests a lower overall coronal temperature in the simulation.

4.2. Brightening Remnant

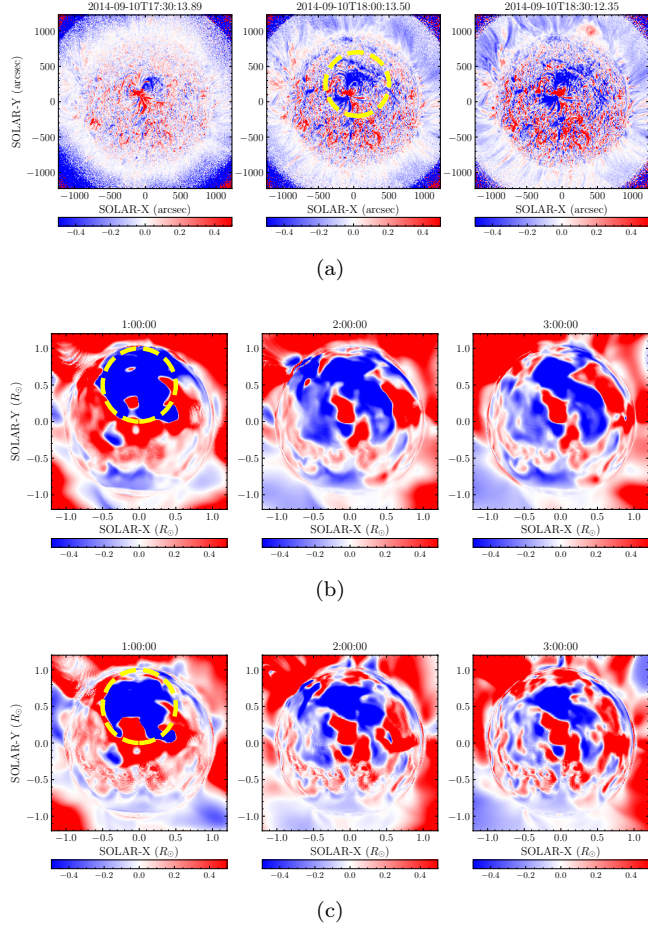


Figure 11. Relative intensity change in SDO/AIA 171 Å passband before and after the eruption in observation (a), PF0.37 model (b), and PF1.0 model (c). The yellow circles illustrate the position of the AR 12158 and the ambient solar corona.

An unexpected brightening remnant is shown in synthetic LASCO C2 and C3 images after the eruption of the CME leading edge. To understand the brightening structure's formation, I show the solar wind property at 5h50m after the CME eruption in the PF1.0 model at $z = 0$ in Figure 14. The brightening structures in LASCO FOV corresponds to the density enhancement and low proton temperature region at $X \sim -5 R_{\odot}$ and $Y \sim 5 R_{\odot}$, which is a part of "filament plasma" embedded in the flux rope. The structure does not erupt into the solar wind successfully and falls back to the solar corona. I guess the failed eruption of the "filament plasma" in the simulation may be related to the magnetic field strength in the inserted flux rope.

4.3. CME Radial Speed

The propagation speed of the simulated CME shocks in PF0.37 and PF1.0 models are all slower than observa-

tions. The simulated CME shock in the PF0.37 model arrives at the earth 12 hours later, and in the PF1.0 model it arrives at the earth three days later. The delay of CME arrival is associated with two factors in the simulation: the steady-state solar wind density and the magnetic field strength in the flux rope.

The ambient solar wind density, especially in the PF1.0 model, is much larger than the observed value from the OMNI database, making the CME acceleration in solar corona and inner heliosphere less efficient. The main reason for the deviation in the background solar wind density may come from the GONG synoptic map. Sachdeva et al. (2019) reported that using a GONG map processed with Air Force Data Assimilative Photospheric flux Transport (ADAPT, Henney et al. 2012) produces much better steady-state solar wind conditions than only using GONG synoptic map.

The CME speed near the sun constrains the field strength in the flux rope. Jin et al. (2017a) mentioned that successive runs are needed to obtain a proper field strength to provide the best overall propagation time. Sometimes, the CME propagation speed near the sun is set to be slightly larger than the observed values to balance the denser ambient solar wind (Jin et al. 2017a). Since this is only a class project, I do not have enough time to perform the optimization study for the flux rope field strength. The field strength provided by EEGGL is directly used in the simulation.

5. CONCLUSIONS

In this project, I am assigned to simulate a halo CME that erupted on September 10, 2014, using Alfvén Wave Solar Wind Model (AWSOM) and Eruptive Events Generator, Gibson and Low (EEGGL). I used the synoptic photospheric magnetogram from Global Oscillation Network Group (GONG) to obtain two steady-state solar wind solutions of CR2154 with different Poynting flux: PF0.37 model with a Poynting flux constant of 0.37×10^6 and PF1.0 with a constant of $10^6 \text{ J} \cdot \text{m}^{-2} \cdot \text{s}^{-1} \cdot \text{T}^{-1}$. The synthetic solar EUV images and solar wind conditions at 1 au are compared with SDO, STEREO, and OMNI data. The solar EUV corona in both models is fainter than the observations from SDO/AIA and STEREO/SECCHI EUVI, especially the PF0.37 model with smaller Poynting flux at the inner boundary. The PF0.37 model produces better solar wind conditions at 1 au when compared with observed values. The solar wind density in PF1.0 is much higher than the OMNI data.

After that, I used the EEGGL to obtain the CME flux rope parameters and insert the flux rope in the steady-state solar wind solutions. Both models can reproduce

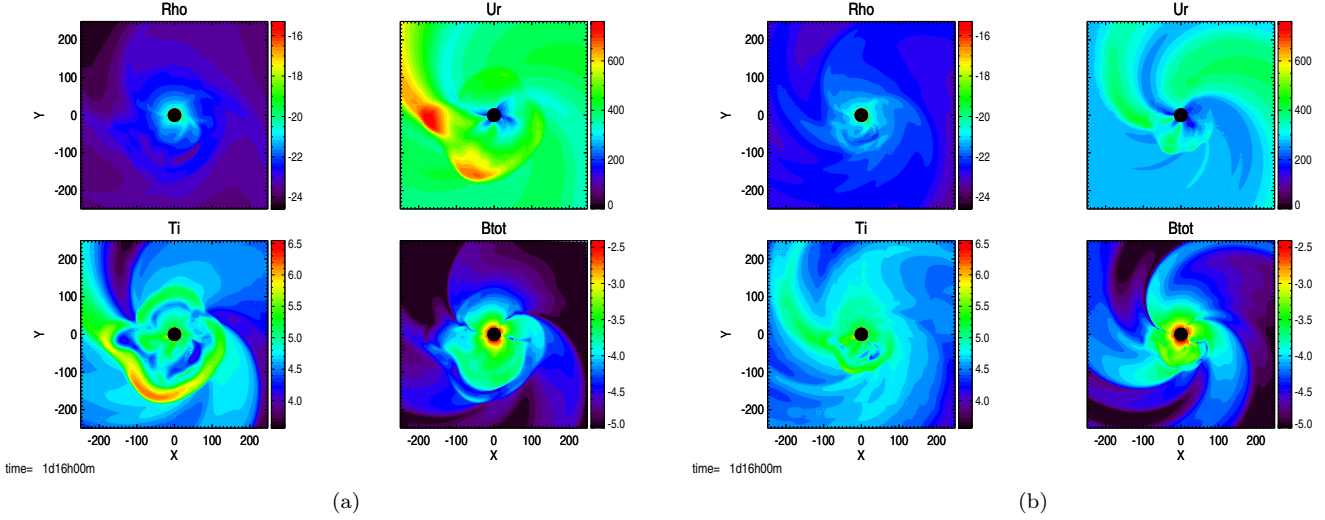


Figure 12. CME shock and ambient solar wind condition at the equatorial plane ($z = 0$) 40 h after the CME eruption in PF0.37 (a) and PF1.0 (b) model: Mass density ($\text{g} \cdot \text{cm}^{-3}$), radial velocity ($\text{km} \cdot \text{s}^{-1}$), proton temperature (K), total magnetic field strength (G).

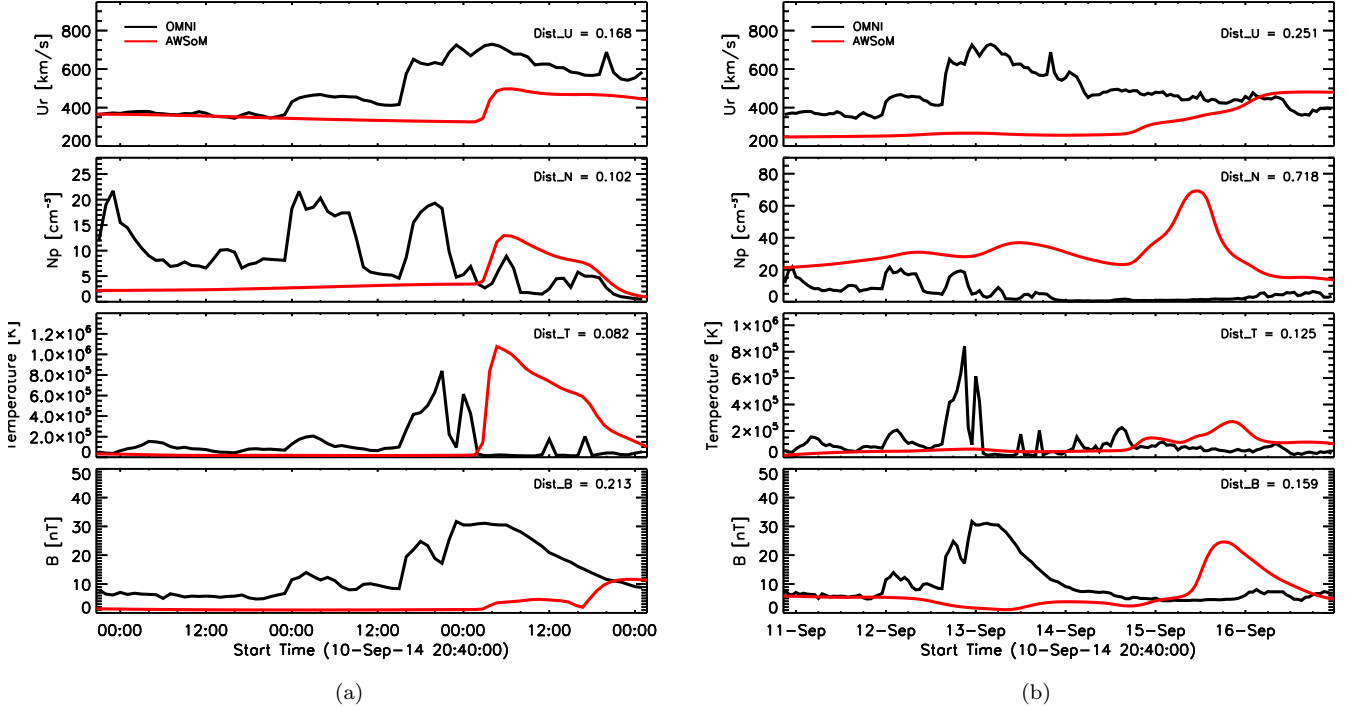


Figure 13. Comparison between the solar wind condition from PF0.37 (a) and PF1.0 (b) CME simulations with OMNI database.

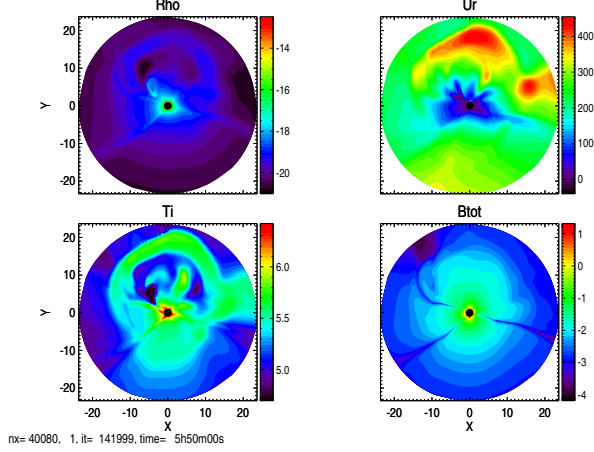


Figure 14. CME properties in the solar corona at 5h50m after the eruption in the equatorial cut ($z = 0$).

the brightening leading edge of the CME eruption observed in LASCO C2 and C3. However, the CME propagation speed in PF1.0 model is much slower than the observations. An unexpected brightening structure, which corresponds to a part of flux rope plasma that does not eject successfully into the interplanetary space, can be found in synthetic LASCO C2 and C3 images. The AWM simulation can reproduce the similar corona dimming patterns observed in SDO/AIA 171 Å passband. In the PF0.37 model, the CME shock arrives at the earth 12 hours later than the observations. The CME propagates more slowly in the PF1.0 model than the propagation in the PF0.37 model due to the denser ambient solar wind. The jump of radial velocity and number density when crossing the CME shock in PF0.37 model is smaller than the observed values, while the proton temperature jump is more enormous. In the PF1.0 model, it takes the CME shock three more days to arrive at the earth in the simulation. The density jump in PF1.0 model is much larger than the OMNI data, while the proton temperature jump is much smaller due to the slow propagation speed.

To improve the simulation results in the future, we can use ADAPT-GONG map to obtain the potential field at the inner boundary and optimize the flux rope field strength by successive runs. In the future, we can investigate some other topics, which are not covered in this project, e.g., synthesizing Hinode/EIS observations of the eruption, monitoring the ion charge state evolution during the CME propagation from the sun to 1 au, and simulating the Cryogenic Near-Infrared Spectropolarimeter (Cryo-NIRSP) mounted on the newly-built Daniel K. Inouye Solar Telescope (DKIST, Rimmele et al. 2020).

ACKNOWLEDGEMENTS

Y.Z. acknowledges the help of Dr. Zhenguang Huang, Dr. Nishtha Sachdeva, and Dr. Gábor Tóth in running AWM and EEGGL on Cheyenne and post-processing of the simulation results. Y.Z. would also like to thank Prof. Tamas Gombosi for giving the SPACE 597 lectures and providing an excellent opportunity to run AWM simulations. Y.Z. also acknowledges the help of the other students working on the SPACE 597 projects. They are Austin Brenner, Shannon Hill, Daniel Carpenter, and Paige Cooley.

The Eruptive Event generator (EE), Solar Corona (SC), Inner Heliosphere (IH) components of SWMF are based on BATSRUS MHD code developed at the Center for Space Environment Modeling (CSEM). BATSRUS is a highly parallel up to 3-dimensional block-adaptive hydrodynamic and MHD code. Currently, the main developers of BATSRUS are Gabor Toth, Bart van der Holst, and Igor Sokolov. The current version of the Solar Corona model was developed by Bart van der Holst, Chip Manchester, Igor Sokolov with contributions from Cooper Downs, Ilia Roussev, and Ofer Cohen. The Inner Heliosphere model was mostly developed by Chip Manchester. The physics-based Eruptive Even Generator model is also based on BATSRUS. It is developed by Fang Fang, Chip Manchester, and Bart van der Holst. The EE model already works as a stand-alone code, and it will be coupled to other components in the SWMF in the future.

Y.Z. would like to acknowledge high-performance computing support from Cheyenne (<https://doi.org/10.5065/D6RX99HX>) provided by NCAR's Computational and Information Systems Laboratory, sponsored by the National Science Foundation.

This work utilizes data obtained by the Global Oscillation Network Group (GONG) program, managed by the National Solar Observatory, which is operated by auRA, Inc. under a cooperative agreement with the National Science Foundation. The data were acquired by instruments operated by the Big Bear Solar Observatory, High Altitude Observatory, Learmonth Solar Observatory, Udaipur Solar Observatory, Instituto de Astrofísica de Canarias, and Cerro Tololo Interamerican Observatory. Data supplied courtesy of the SDO/AIA consortia. SDO is the first mission to be launched for NASA's Living With a Star (LWS) Program. Full-disk EUVI images are supplied courtesy of the STEREO Sun Earth Connection Coronal and Heliospheric Investigation (SECCHI) team. We acknowledge use of NASA/GSFC's Space Physics Data Facility's OMNI-Web (or CDAWeb or ftp) service, and OMNI data. The SOHO/LASCO data used here are produced by a con-

soritum of the Naval Research Laboratory (USA), Max-Planck-Institut fuer Aeronomie (Germany), Laboratoire d'Astronomie (France), and the University of Birmingham (UK). SOHO is a project of international cooperation between ESA and NASA. The SDO/AIA and SOHO/LASCO level 0.5 data are downloaded from the Virtual Solar Observatory (VSO). The VSO project is led by Dr. Frank Hill at NSO. VSO is a research tool

that allows scientists to search for solar and heliospheric physics data.

Software: Numpy (Oliphant 2006; Van Der Walt et al. 2011), Scipy (Virtanen et al. 2020), Astropy (Astropy Collaboration et al. 2013; Price-Whelan et al. 2018), Sunpy (The SunPy Community et al. 2020), sunkit_image (<https://github.com/sunpy/sunkit-image>), Matplotlib (Hunter 2007), SolarSoft (<https://www.lmsal.com/solarsoft>), num2tex (<https://github.com/AndrewChap/num2tex>), Science Plots (Garrett 2020).

APPENDIX

A. SOHO/LASCO DATA REDUCTION

Unfortunately, there is no one-line script to read the synthetic SOHO/LASCO C2 and C3 outputs of AWSoM and compare them with the observations, partly because of the complicated data reduction procedures unlike the straightforward `aia_prep` for SDO/AIA data. The CME structures are usually dominated by the strong emission from the F (dust) corona and static K (electron) corona. In the main body of the paper, I directly used the data products (actually JPEG images) from the Helioviewer since they have better contrast to show the CME structures.

I also tried some methods to enhance the CME structures observed in the LASCO C2 coronagraph. The data reduction and processing are described as follows:

1. The SOHO/LASCO C2 level 0.5 data are downloaded from the Virtual Solar Observatory (VSO).
2. I used the `reduce_level_1.pro` in SSWIDL to calibrate the level 0.5 data to level 1.
3. A monthly minimum background model downloaded from the NRL website is calibrated to level 1 and subtracted from the level 1 data to remove the dominant static K-corona, F-corona, and stray light (Morrill et al. 2006).

After that, I used two ways to enhance the image furthermore. One is to calculate the ratio between the white-light images during eruption and the daily median image. The other is adopting a Normalized Radial Graded Filter (NRGF, Morgan et al. 2006) provided in sunkit_image to filter the static K-corona which has a steep gradient along the radial direction. The results are shown in Figure 15. The raw level-1 image in the first row is dominated by F-corona emission, and barely any K-corona structures can be distinguished. The background model subtraction reveals the fine streamers in

the K-corona and part of the CME leading edge. The white-light ratio images enhance the CME leading edge and the halo shaped ambient regions, while some of the streamers appear to be dark. The images filtered by NRGF also reveal the fine structures in the CME eruption and the dark cavity behind the leading edge. The enhancement in the lower-left corner should be an artificial effect.

B. BUGS AND SOLUTIONS

In this section, I list the major errors and problems that I encountered during the AWSoM runs and the solutions:

1. The `make rundir` command cannot generate the IH and SC directory in the run directory. Solution: use the run directory generated by `test9`.
2. SWMF crashed when reading the FDIPS processed magnetogram without any error messages. Solution: add `-grid uniform` keyword after `./remap_magnetogram.py` to convert the magnetogram into uniform (co)latitude grid.
3. Error message in steady-state time stepping: `NaN` in variables `-rho`. Solution: use `#MINIMUMRADIALSPEED` command in `PARAM.in` to avoid inflows in solar wind.
4. `GLSETUP.py` cannot show interactive GUI to select the position of the footprints remotely. Solution: determine the position of the footprints from the EEGGL on CCMC website, then pass them to the `GLSETUP.py` by:
`GLSETUP.py InputfitsFileName -CMESpeed
InputSpeed -LonPosIn LonPos -LatPosIn
LatPos -LonNegIn LatNeg -LatNegIn LatNeg`

And I found the `README` file in `SWMF/share/IDL/Solar/` does not have a detailed description for the setup of the

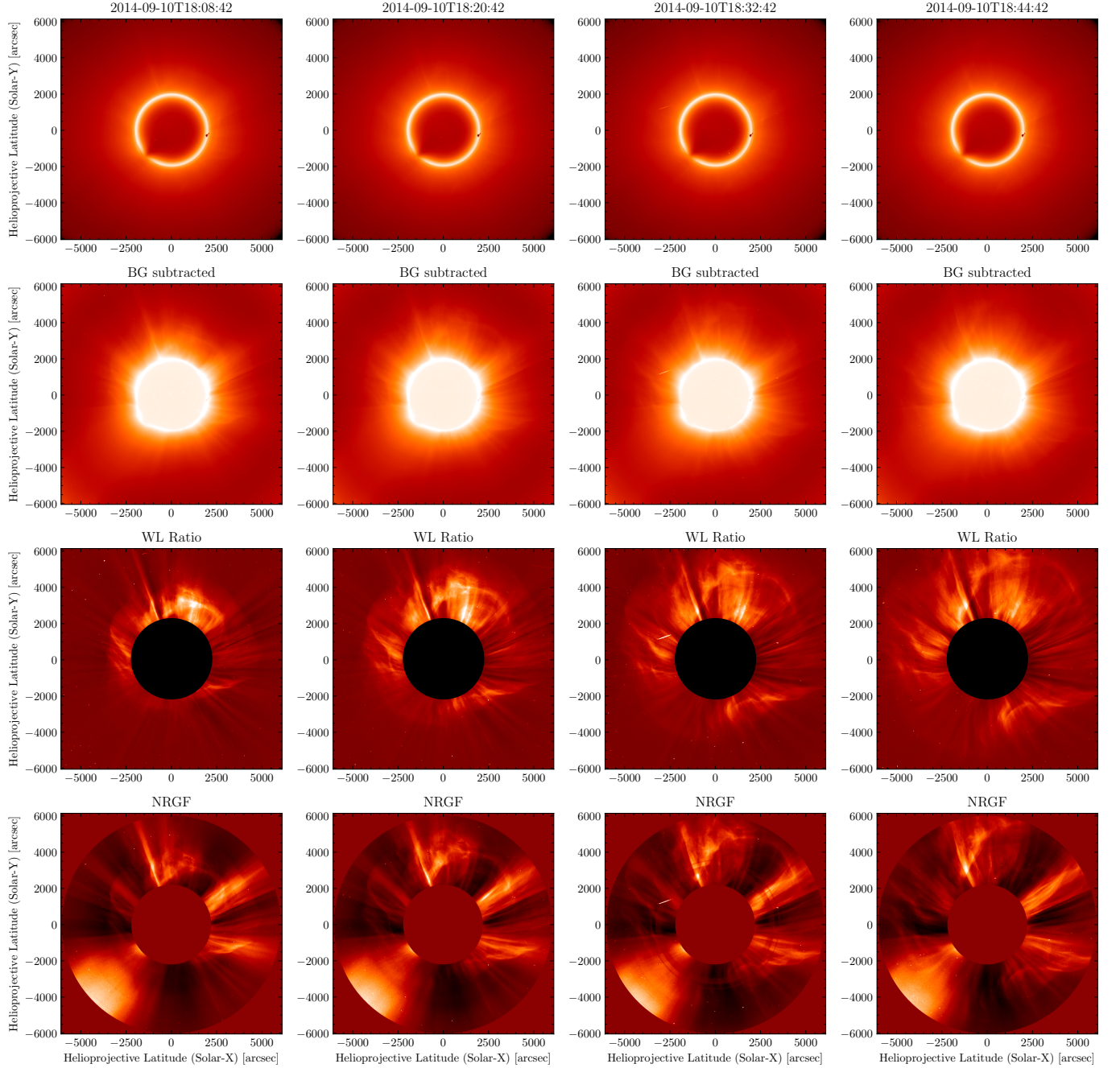


Figure 15. First row: SOHO/LASCO C2 white-light level 1 data during CME eruption plotted in log scale; Second row: SOHO/LASCO C2 white-light level 1 data with background model subtracted plotted in log scale; Third row: white-light ratio between the CME images and the daily median value; Last row: SOHO/LASCO C2 level 1 data after NRGF processing

`compare_remote.pro` and `compare_insu.pro` script.
So I also write down my procedures and encountered problems here:

1. Include the `SWMF/share/IDL/share/General` into the IDL path by `setenv IDL_PATH ...` or `export IDL_PATH=...` (see the SWMF IDL documentation).
2. Copy the `los_*.out` and `*.sat` files to `SWMF/share/IDL/Solar/simdata` directory
3. Change the first line in `setenv_insu.sh` and `setenv_remote.sh` to `setenv <ssw_path>` where `<ssw_path>` is the location where the SSW is installed (by default `/usr/local/ssw`).

4. Run `setenv_remote.sh` or `setenv_insitu.sh` and then run `compare_remote.pro` and `compare_insitu.pro` in the IDL command line.

Some problems and solutions:

1. When running `compare_remote`, IDL cannot find procedure `compare_AIA` or `compare_EUV`, that's because at some machines IDL can only recognize procedure names in lower case, one can either compile them manually or add these lines to the `ssw_startup_remote` file:

```
.compile compare_AIA
.compile compare_EUV

2. When running compare_remote, there's an error message DS_MPO. That's because the AIA team updated the aia_prep procedure in SSW in 2019. If you are using SSW installed or updated after 2019, open the procedures_local.pro, search "aia_prep" (or go to line 782), add another keyword /no_mpo_update at the end of that line, i.e.  

aia_prep, filename, -1, index, data,$  

/normalize, /no_mpo_update
```

REFERENCES

- Amari, T., Luciani, J. F., Aly, J. J., Mikic, Z., & Linker, J. 2003a, ApJ, 585, 1073, doi: [10.1086/345501](https://doi.org/10.1086/345501)
- . 2003b, ApJ, 595, 1231, doi: [10.1086/377444](https://doi.org/10.1086/377444)
- Antiochos, S. K., DeVore, C. R., & Klimchuk, J. A. 1999, ApJ, 510, 485, doi: [10.1086/306563](https://doi.org/10.1086/306563)
- Aschwanden, M. J. 2019, Astrophysics and Space Science Library, Vol. 458, New Millennium Solar Physics, doi: [10.1007/978-3-030-13956-8](https://doi.org/10.1007/978-3-030-13956-8)
- Astropy Collaboration, Robitaille, T. P., Tollerud, E. J., et al. 2013, A&A, 558, A33, doi: [10.1051/0004-6361/201322068](https://doi.org/10.1051/0004-6361/201322068)
- Bein, B. M., Berkebile-Stoiser, S., Veronig, A. M., et al. 2011, ApJ, 738, 191, doi: [10.1088/0004-637X/738/2/191](https://doi.org/10.1088/0004-637X/738/2/191)
- Brueckner, G. E., Howard, R. A., Koomen, M. J., et al. 1995, SoPh, 162, 357, doi: [10.1007/BF00733434](https://doi.org/10.1007/BF00733434)
- Chen, P. F. 2011, Living Reviews in Solar Physics, 8, 1, doi: [10.12942/lrsp-2011-1](https://doi.org/10.12942/lrsp-2011-1)
- Chen, P. F., & Shibata, K. 2000, ApJ, 545, 524, doi: [10.1086/317803](https://doi.org/10.1086/317803)
- Cheng, X., Guo, Y., & Ding, M. 2017, Science China Earth Sciences, 60, 1383, doi: [10.1007/s11430-017-9074-6](https://doi.org/10.1007/s11430-017-9074-6)
- Cohen, O., Attrill, G. D. R., Manchester, Ward B., I., & Wills-Davey, M. J. 2009, ApJ, 705, 587, doi: [10.1088/0004-637X/705/1/587](https://doi.org/10.1088/0004-637X/705/1/587)
- Cohen, O., Attrill, G. D. R., Schwadron, N. A., et al. 2010, Journal of Geophysical Research (Space Physics), 115, A10104, doi: [10.1029/2010JA015464](https://doi.org/10.1029/2010JA015464)
- Cohen, O., Sokolov, I. V., Roussev, I. I., et al. 2008, Journal of Atmospheric and Solar-Terrestrial Physics, 70, 583, doi: [10.1016/j.jastp.2007.08.065](https://doi.org/10.1016/j.jastp.2007.08.065)
- Domingo, V., Fleck, B., & Poland, A. I. 1995, SoPh, 162, 1, doi: [10.1007/BF00733425](https://doi.org/10.1007/BF00733425)
- Garrett, J. D. 2020, doi: [10.5281/zenodo.4106650](https://doi.org/10.5281/zenodo.4106650)
- Gibson, S. E., & Low, B. C. 1998, ApJ, 493, 460, doi: [10.1086/305107](https://doi.org/10.1086/305107)
- Groth, C. P. T., De Zeeuw, D. L., Gombosi, T. I., & Powell, K. G. 2000, J. Geophys. Res., 105, 25053, doi: [10.1029/2000JA900093](https://doi.org/10.1029/2000JA900093)
- Harvey, J. W., Hill, F., Hubbard, R. P., et al. 1996, Science, 272, 1284, doi: [10.1126/science.272.5266.1284](https://doi.org/10.1126/science.272.5266.1284)
- Henney, C. J., Toussaint, W. A., White, S. M., & Arge, C. N. 2012, Space Weather, 10, doi: [10.1029/2011SW000748](https://doi.org/10.1029/2011SW000748)
- Howard, R. A., Moses, J. D., Vourlidas, A., et al. 2008, SSRv, 136, 67, doi: [10.1007/s11214-008-9341-4](https://doi.org/10.1007/s11214-008-9341-4)
- Hunter, J. D. 2007, Computing in Science & Engineering, 9, 90, doi: [10.1109/MCSE.2007.55](https://doi.org/10.1109/MCSE.2007.55)
- Illing, R. M. E., & Hundhausen, A. J. 1985, J. Geophys. Res., 90, 275, doi: [10.1029/JA090iA01p00275](https://doi.org/10.1029/JA090iA01p00275)
- Jacobs, C., Poedts, S., & van der Holst, B. 2006, A&A, 450, 793, doi: [10.1051/0004-6361:20054670](https://doi.org/10.1051/0004-6361:20054670)
- Jin, M., Manchester, W. B., van der Holst, B., et al. 2017a, ApJ, 834, 172, doi: [10.3847/1538-4357/834/2/172](https://doi.org/10.3847/1538-4357/834/2/172)
- Jin, M., Schrijver, C. J., Cheung, M. C. M., et al. 2016, ApJ, 820, 16, doi: [10.3847/0004-637X/820/1/16](https://doi.org/10.3847/0004-637X/820/1/16)
- Jin, M., Manchester, W. B., van der Holst, B., et al. 2013, ApJ, 773, 50, doi: [10.1088/0004-637X/773/1/50](https://doi.org/10.1088/0004-637X/773/1/50)
- . 2017b, ApJ, 834, 173, doi: [10.3847/1538-4357/834/2/173](https://doi.org/10.3847/1538-4357/834/2/173)
- Kaiser, M. L., Kucera, T. A., Davila, J. M., et al. 2008, SSRv, 136, 5, doi: [10.1007/s11214-007-9277-0](https://doi.org/10.1007/s11214-007-9277-0)
- Kliem, B., & Török, T. 2006, PhRvL, 96, 255002, doi: [10.1103/PhysRevLett.96.255002](https://doi.org/10.1103/PhysRevLett.96.255002)
- Lemen, J. R., Title, A. M., Akin, D. J., et al. 2012, SoPh, 275, 17, doi: [10.1007/s11207-011-9776-8](https://doi.org/10.1007/s11207-011-9776-8)
- Lin, J., Forbes, T. G., Isenberg, P. A., & Démoulin, P. 1998, ApJ, 504, 1006, doi: [10.1086/306108](https://doi.org/10.1086/306108)

- Lugaz, N., Downs, C., Shibata, K., et al. 2011, ApJ, 738, 127, doi: [10.1088/0004-637X/738/2/127](https://doi.org/10.1088/0004-637X/738/2/127)
- Lugaz, N., Farrugia, C. J., Manchester, W. B., I., & Schwadron, N. 2013, ApJ, 778, 20, doi: [10.1088/0004-637X/778/1/20](https://doi.org/10.1088/0004-637X/778/1/20)
- Lugaz, N., Manchester, W. B., I., & Gombosi, T. I. 2005a, ApJ, 627, 1019, doi: [10.1086/430465](https://doi.org/10.1086/430465)
- . 2005b, ApJ, 634, 651, doi: [10.1086/491782](https://doi.org/10.1086/491782)
- Lugaz, N., Manchester, W. B., I., Roussev, I. I., Tóth, G., & Gombosi, T. I. 2007, ApJ, 659, 788, doi: [10.1086/512005](https://doi.org/10.1086/512005)
- Manchester, W. B., I., van der Holst, B., & Lavraud, B. 2014a, Plasma Physics and Controlled Fusion, 56, 064006, doi: [10.1088/0741-3335/56/6/064006](https://doi.org/10.1088/0741-3335/56/6/064006)
- Manchester, W. B., I., van der Holst, B., Tóth, G., & Gombosi, T. I. 2012, ApJ, 756, 81, doi: [10.1088/0004-637X/756/1/81](https://doi.org/10.1088/0004-637X/756/1/81)
- Manchester, Ward B., I., Vourlidas, A., Tóth, G., et al. 2008, ApJ, 684, 1448, doi: [10.1086/590231](https://doi.org/10.1086/590231)
- Manchester, W., van der Holst, B., Jin, M., & Kasper, J. C. 2019, in AGU Fall Meeting Abstracts, Vol. 2019, SH41A-04
- Manchester, W. B., Gombosi, T. I., Roussev, I., et al. 2004a, Journal of Geophysical Research (Space Physics), 109, A01102, doi: [10.1029/2002JA009672](https://doi.org/10.1029/2002JA009672)
- . 2004b, Journal of Geophysical Research (Space Physics), 109, A02107, doi: [10.1029/2003JA010150](https://doi.org/10.1029/2003JA010150)
- Manchester, W. B., Kozyra, J. U., Lepri, S. T., & Lavraud, B. 2014b, Journal of Geophysical Research (Space Physics), 119, 5449, doi: [10.1002/2014JA019882](https://doi.org/10.1002/2014JA019882)
- Mason, J. P., Woods, T. N., Caspi, A., Thompson, B. J., & Hock, R. A. 2014, ApJ, 789, 61, doi: [10.1088/0004-637X/789/1/61](https://doi.org/10.1088/0004-637X/789/1/61)
- Moore, R. L., & Labonte, B. J. 1980, in Solar and Interplanetary Dynamics, ed. M. Dryer & E. Tandberg-Hanssen, Vol. 91, 207–210
- Morgan, H., Habbal, S. R., & Woo, R. 2006, SoPh, 236, 263, doi: [10.1007/s11207-006-0113-6](https://doi.org/10.1007/s11207-006-0113-6)
- Morrill, J. S., Korendyke, C. M., Brueckner, G. E., et al. 2006, SoPh, 233, 331, doi: [10.1007/s11207-006-2058-1](https://doi.org/10.1007/s11207-006-2058-1)
- Oliphant, T. E. 2006, A guide to NumPy, Vol. 1 (Trelgol Publishing USA)
- Pesnell, W. D., Thompson, B. J., & Chamberlin, P. C. 2012, SoPh, 275, 3, doi: [10.1007/s11207-011-9841-3](https://doi.org/10.1007/s11207-011-9841-3)
- Powell, K. G., Roe, P. L., Linde, T. J., Gombosi, T. I., & De Zeeuw, D. L. 1999, Journal of Computational Physics, 154, 284, doi: [10.1006/jcph.1999.6299](https://doi.org/10.1006/jcph.1999.6299)
- Price-Whelan, A. M., Sipőcz, B. M., Günther, H. M., et al. 2018, AJ, 156, 123, doi: [10.3847/1538-3881/aabc4f](https://doi.org/10.3847/1538-3881/aabc4f)
- Riley, P., Linker, J. A., Mikić, Z., et al. 2003, Journal of Geophysical Research (Space Physics), 108, 1272, doi: [10.1029/2002JA009760](https://doi.org/10.1029/2002JA009760)
- Rimmele, T. R., Warner, M., Keil, S. L., et al. 2020, SoPh, 295, 172, doi: [10.1007/s11207-020-01736-7](https://doi.org/10.1007/s11207-020-01736-7)
- Roussev, I. I., Forbes, T. G., Gombosi, T. I., et al. 2003, ApJL, 588, L45, doi: [10.1086/375442](https://doi.org/10.1086/375442)
- Sachdeva, N., van der Holst, B., Manchester, W. B., et al. 2019, ApJ, 887, 83, doi: [10.3847/1538-4357/ab4f5e](https://doi.org/10.3847/1538-4357/ab4f5e)
- Sakurai, T. 1976, PASJ, 28, 177
- Schrijver, C. J., DeRosa, M. L., Metcalf, T., et al. 2008, ApJ, 675, 1637, doi: [10.1086/527413](https://doi.org/10.1086/527413)
- The SunPy Community, Barnes, W. T., Bobra, M. G., et al. 2020, The Astrophysical Journal, 890, 68, doi: [10.3847/1538-4357/ab4f7a](https://doi.org/10.3847/1538-4357/ab4f7a)
- Tian, H., McIntosh, S. W., Xia, L., He, J., & Wang, X. 2012, ApJ, 748, 106, doi: [10.1088/0004-637X/748/2/106](https://doi.org/10.1088/0004-637X/748/2/106)
- Titov, V. S., & Démoulin, P. 1999, A&A, 351, 707
- Török, T., & Kliem, B. 2003, A&A, 406, 1043, doi: [10.1051/0004-6361:20030692](https://doi.org/10.1051/0004-6361:20030692)
- Tóth, G., van der Holst, B., & Huang, Z. 2011, ApJ, 732, 102, doi: [10.1088/0004-637X/732/2/102](https://doi.org/10.1088/0004-637X/732/2/102)
- Tóth, G., Sokolov, I. V., Gombosi, T. I., et al. 2005, Journal of Geophysical Research (Space Physics), 110, A12226, doi: [10.1029/2005JA011126](https://doi.org/10.1029/2005JA011126)
- Tóth, G., van der Holst, B., Sokolov, I. V., et al. 2012, Journal of Computational Physics, 231, 870, doi: [10.1016/j.jcp.2011.02.006](https://doi.org/10.1016/j.jcp.2011.02.006)
- van der Holst, B., Manchester, W. B., I., Frazin, R. A., et al. 2010, ApJ, 725, 1373, doi: [10.1088/0004-637X/725/1/1373](https://doi.org/10.1088/0004-637X/725/1/1373)
- van der Holst, B., Sokolov, I. V., Meng, X., et al. 2014, ApJ, 782, 81, doi: [10.1088/0004-637X/782/2/81](https://doi.org/10.1088/0004-637X/782/2/81)
- Van Der Walt, S., Colbert, S. C., & Varoquaux, G. 2011, Computing in Science & Engineering, 13, 22
- Virtanen, P., Gommers, R., Oliphant, T. E., et al. 2020, Nature Methods, 17, 261, doi: <https://doi.org/10.1038/s41592-019-0686-2>
- Vourlidas, A., Howard, R. A., Esfandiari, E., et al. 2010, ApJ, 722, 1522, doi: [10.1088/0004-637X/722/2/1522](https://doi.org/10.1088/0004-637X/722/2/1522)
- Webb, D. F., & Howard, T. A. 2012, Living Reviews in Solar Physics, 9, 3, doi: [10.12942/lrsp-2012-3](https://doi.org/10.12942/lrsp-2012-3)
- Yan, Y., Aschwanden, M. J., Wang, S., & Deng, Y. 2001, SoPh, 204, 27, doi: [10.1023/A:1014265123601](https://doi.org/10.1023/A:1014265123601)